INTERNATIONAL JOURNAL OF HYDROGEN ENERGY 47 (2022) 27787–27799

Available online at www.sciencedirect.com

ScienceDirect

journal homepage: www.elsevier.com/locate/he

Thermo-fluid dynamics modelling of steam electrolysis in fully-assembled tubular high-temperature proton-conducting cells

D. Catalán-Martínez [a], L. Navarrete [a], M. Tarach [a], J. Santos-Blasco [a], E. Vøllestad [b], T. Norby [c], M.I. Budd [d], P. Veenstra [e], J.M. Serra [a,*]

[a] Instituto de Tecnología Química (Universitat Politècnica de València—Consejo Superior de Investigaciones Científicas), Valencia, Spain

[b] SINTEF Industry, Sustainable Energy Technology, Oslo, Norway

[c] Department of Chemistry, Centre for Materials Science and Nanotechnology (SMN), University of Oslo, Oslo, Norway

[d] CoorsTek Membrane Sciences AS, Oslo, Norway

[e] Shell Global Solutions International B.V, Netherlands

HIGHLIGHTS

- A complete thermo-CFD model was built for a compact proton-ceramic steam electrolysis unit.
- The thermoneutral voltage at a specific steam conversion is a key indicator of the electrolysis unit performance.
- The selection of a porous medium for the electronic current collector favours heat transfer.
- The operation under different operating conditions does not present with no fluid or thermal limitations.

GRAPHICAL ABSTRACT

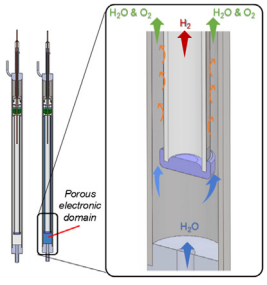

ARTICLE INFO

Article history:
Received 15 March 2022
Received in revised form
9 June 2022
Accepted 12 June 2022
Available online 22 July 2022

ABSTRACT

Electrolysis based on renewable energies offers a promising carbon-free solution for hydrogen generation and storage. The recent developments of proton ceramic electrolysis cells operating at intermediate temperatures bear promise of superior energy efficiency compared to oxide ion conducting electrolytes. Here, a proton ceramic Single Engineering Unit (SEU) design is optimized for steam electrolysis using a computational fluid dynamics (CFD) model implemented in a COMSOL Multiphysics software. The SEU is an all-in-one tubular cell arrangement that constitutes the smallest electrolysis unit and enables efficient, adaptable pressurized hydrogen generation. The parametrical modelling study is

* Corresponding author.
E-mail addresses: jmserra@itq.upv.es, jm_serra@hotmail.com (J.M. Serra).

https://doi.org/10.1016/j.ijhydene.2022.06.112

Keywords:
Ceramic proton conductor
CFD
Tubular cell
Water electrolysis
Modelling

conducted for two adiabatic operation scenarios with distinct steam conversion rates and tested for multiple key parameters, namely internal and external chamber pressures and inlet stream temperature. The modelling results show that low steam conversions enable operation at higher current densities and that the thermoneutral voltage for a fixed steam conversion is highly sensitive to the process conditions and operation modes. The increment of the pressure of the generated hydrogen implies a reduced production rate at thermoneutral voltage, although it can be compensated with an enhanced steam pressure or a reduced inlet temperature. Additionally, the introduction of a porous medium as the SEU current collector in the steam chamber enhances heat transport within this chamber. The area specific resistance of the system determines the current density, enforcing an adaption of the area of the electrolyser to satisfy the target hydrogen production and energy efficiency. The resulting proposed SEU design and adapted operational parameters allow effective delivery of pressurized dry hydrogen for a wide range of conditions and applications.

Introduction

The escalating climate change warning signs added to the environmental legislation stringency urges the development of renewable, carbon-free alternatives to current energy sources and technologies [1,2]. Hydrogen from electrolysis may replace fossil fuels and represents a clean burning energy carrier [3] with high gravimetric energy density (143 MJ kg^{-1}), while storage and application may suffer from its low volumetric energy density [4,5]. Furthermore, hydrogen from fossil sources involves considerable CO_2 emissions (around 8–12 kg CO_2 eq/kg H_2) ascribed to production by reforming fossil feedstocks [2,6–10]. Electrolysis is an attractive alternative for hydrogen production due to its low CO_2 footprint and potential for small scale production which only requires water and electricity [9]. Recent developments on Pt-based catalysts and metal-organic frameworks (MOFs) have displayed high performance and versatility compared to previous systems [11–15]. Currently, the high cost of electrolysis prevents its full commercialization, and further efforts are required to increase its economic viability. Since the cost of electrolysis originates mainly from its large electrical demands, there has recently been much interest related to the integration of lower cost renewable energy sources to power electrolysis systems to produce green hydrogen [3,16,17]. Due to this increasing availability of renewable power and the raising green H_2 demand for transport and industrial purposes [17–21], various Power-to-Gas (P2G) projects have emerged with this objective. Electrolysis systems would provide a zero-emission pathway from renewable energy to hydrogen for use in energy generation or to produce added value compounds.

High temperature electrolysers based on ion-conducting ceramic electrolytes possess the highest theoretical efficiency, although their commercial release is hardly available [10,22,23]. Proton conducting ceramics operating in the intermediate temperature range (400–700 °C) exhibit in principle higher efficiencies compared to conventional oxide-ion conducting ceramics [24,25]. Additionally, proton ceramic electrolysis cells generate pure, dry hydrogen instead of water-diluted hydrogen produced by oxide-ion conducting electrolysers, which on their side instead generate undiluted and hence hazardous oxygen. Significant progress has been made in development of proton ceramics over the past decade. For example, Vøllestad et al. developed a scalable tubular electrolysis cell based on a proton ceramic electrolyte [26]. New electrolyte materials such as multi-doped barium zirconate have exhibited substantial improvements in performance, however, still only at button single cell scale in the case of electrolysis [27,28].

To better understand high-temperature electrolysis systems, different authors have leveraged a finite-element approach for advanced analysis of related processes [29–33]. Finite elements methodology unfolds a collection of procedures to solve complex differential equations based on the discretization of the geometry. Therefore, this methodology allows obtaining the internal performance of the studied phenomena. This information can be used to improve the understanding on how a process work inside one specific geometry system and to guide the design of a reactor system. When analysing the cell heat balance, three electrolysis operation modes can be considered: (i) endothermic operation, that is, working at lower potentials than that of thermoneutral potential; (ii) isothermal, at thermoneutral potential and (iii) exothermic, working at higher potentials than thermoneutral potential. Each mode is directly related to the balance between the heat demand from the reaction and the heat generated from electrochemical overpotential losses [34–36]. The thermoneutral voltage can be defined as the voltage at which the heat required for the electrolytic water dissociation reaction is provided by the overpotential losses of the electrochemical circuit. The heat transfer may limit the electrochemical performance of the electrolyser, and the electrical conductivities and kinetics of the cell components and interfaces are highly temperature dependent [37].

In this study, a computational fluid-dynamics (CFD) model was developed for a modular electrolysis unit. The

methodology is based on advanced modelling of finite-elements in which all phenomena included in the process are coupled, i.e. gas flow, gas diffusion, electrochemistry and heat transport. The high flexibility of the developed methodology enables responses to different demands. Various sensitivity studies were performed to evaluate process performance through the identification of two relevant operation modes based on the steam utilization and the pressure of the system. This computational work helps leverage the processes from laboratory equipment to industrial scale systems, filling the gap in the upscaling of the technology. In fact, it promotes the design development and optimization throughout the identification of the key performance parameters and system upgrade.

Methodology

This work utilizes a CFD methodology to guide the upscaling of high-temperature electrolysers based on tubular proton ceramic cells. Considering the computational approach of this study, extensive experimental data are not available. The modelling results are validated by an elemental dimensionless model (0D model) that accounts for balances of mass, charge and heat (see Supporting information).

Geometry

The set-up analysed in this study consists of a self-contained modular sub-assembly of the electrolyser, hereinafter Single Engineering Unit (SEU), and comprises a tube-in-shell arrangement that operates in vertical orientation (Fig. 1). In this setup, the free space between the electrode and the external shell must be filled to ensure proper current collection. In order to avoid significant potential losses, a porous medium with high electrical conductivity has been selected for this study. A diverse group of structured materials can be considered for this purpose, i.e. foam, wire-mesh, granulates, balls or a combination.

This SEU (Fig. 1) includes a 200 mm long tubular cell with 9.5 mm outer diameter consisting of a porous inner electrode (1 mm thick) coated with a dense, 25 μm thick $BaZr_{0.7}Ce_{0.2}Y_{0.1}O_{3-\delta}$ electrolyte layer. The external electrode covers the centre-most 190 mm section of the electrolyte. The cell is closed at one end by a moulded glass-ceramic cap and sealed to a steel header at the other end via a segment with a graded coefficient of thermal expansion (*CTE*). This set-up provides an internal chamber (inside the tubular cell) and an external chamber (between the cell and the steel shell).

Steam is injected at the bottom of the external chamber (left in Fig. 1). The exhaust stream, consisting of unreacted steam and O_2 generated by electrolysis, exits at the top of the external chamber through a tube on the side of the top plug/manifold. The internal chamber is filled with metallic wool (Cu or Ni) to provide electrical contact between the central current lead and the internal electrode (this wool is not considered a new body in the model). Hydrogen is generated at the internal electrode and leaves the internal chamber via a T-junction at the top of the steel tube which supports the central current lead feedthrough. There is no sweep gas flow through the internal chamber. The external chamber is, as mentioned above, filled with a porous medium, that serves as current collector.

Fig. 2 shows different detailed views of the SEU. The steam enters the external chamber and crosses the porous electronic collector domain, after the electrolysis of steam, the hydrogen generated in the system is transported as protons through the electrolyte and collected from the internal electrode. The electric current is supplied via the steel shell and reaches the external electrode by crossing the porous domain. Finally, the electric current is collected from the internal electrode and guided back by a copper wire.

CFD model

The computational fluid dynamics model was built using the software COMSOL Multiphysics v5.4. The electrolysis process involves different phenomena related to mass and energy exchange: gas flows and diffusion in the external chamber, heat transport and electrochemical reactions must be considered in the fluid dynamics model. Gas flows are modelled using Navier-Stokes equations and corrected by the Brinkman equations to account for the fast-fluid dynamics in porous media, where the constituent particles are assumed to be spherical for permeability computations. An averaged-mixture set of equations including H_2O and O_2 are employed to model gas diffusion (the Knudsen diffusion contribution is neglected). While the binary gas diffusion coefficient between steam and oxygen is estimated using the Fuller equation, a correction that selects the ratio between the porosity and the tortuosity is introduced for the porous domains, considering a spherical particle geometry. Regarding the heat transfer in the system, the SEU assembly is adiabatic and radiation is neglected. The thermal

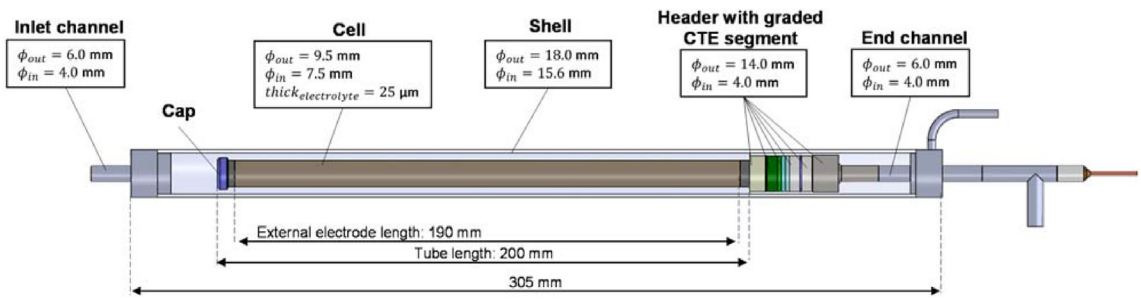

Fig. 1 – View of the SEU tube-in-shell geometry. The SEU is designed to operate in vertical orientation.

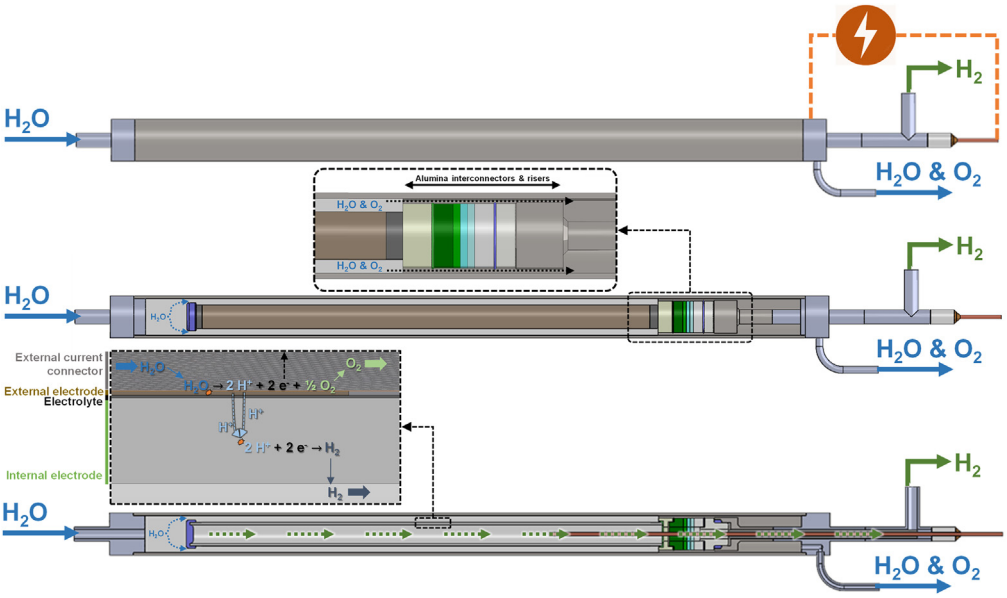

Fig. 2 – View of the SEU tube-in-shell geometry. Blue arrows represent external chamber gas flows while the green arrows represent internal chamber gas flows; orange lines show the electric connection. (For interpretation of the references to color/colour in this figure legend, the reader is referred to the Web version of this article.)

conductivity within the porous domains is also determined taking the estimated porosity into account. All the governing equations employed for the SEU simulation and the properties assumed for the different porous domains of these designs are listed in Tables S1 and S2, respectively (supporting material). In this study, the faradaic efficiency is assumed to be 100% and the Area Specific Resistance (ASR), defined as the overall specific resistance of the electrochemical cell,

$$ASR(T) = ASR_{873K} \cdot \exp\left(-\frac{E_a}{R} \cdot \left(\frac{1}{T} - \frac{1}{873K}\right)\right) \quad (1)$$

is set with a reference value of $ASR_{873K} = 3\ \Omega \cdot cm^2$ and an activation energy of $E_a = 50\ kJ\ mol^{-1}$.

The electrochemical processes are modelled assuming secondary current distribution, with the Butler-Volmer equations governing the electrochemical kinetics [38]. The exchange current density is fixed at $i_0 = 0.1\ A\ cm^{-2}$ and the anodic and cathodic transfer coefficients at $\beta = 0.5$. The complexity of determining a single layer's resistance contribution of the electrochemical cell is overcome by integrating the specific resistance of each layer into a single resistance assigned to the electrolyte layer. This is achieved by minimizing the magnitude of the electrode overpotentials, i.e. by setting high values for the specific ionic and electronic conductivities of the electrodes. Consequently, the ionic conductivity of the electrolyte layer can be estimated as the ratio between its thickness and the ASR. The porous electronic domain was also simplified assuming a solid domain and introducing an electric conductivity of 250 S/cm. The effect of the partial pressures of the external chamber on the reversible potential, E_{rev}, can be accounted for with

$$E_{rev,1} = \frac{\Delta G}{z \cdot F} = \frac{\Delta G_{H2}(T, p_{int}) + 0.5 \cdot \Delta G_{O2}(T, p_{ext}) - \Delta G_{H2O}(T, p_{ext})}{z \cdot F} \quad (2)$$

$$E_{rev} = E_{rev,1} + \frac{R \cdot T}{z \cdot F} \cdot \ln\left(\frac{p_{O2}^{0.5} \cdot p_{H2}}{p_{H2O}}\right) \quad (3)$$

where p_i represents the partial pressure of the i compound.

The model assumes that the external half-reaction ($H_2O \rightarrow 2\,H^+ + 2\,e^- + \frac{1}{2}\,O_2$) is disposed homogeneously throughout the entire external electrode domain and the gas density for the steam and oxygen mixture to be ideal. Additionally, their viscosity and thermal conductivities are calculated using the Wilke model and their heat capacities are obtained as the molar average of each pure component. Analogously, the hydrogen release reaction ($2\,H^+ + 2\,e^- \rightarrow H_2$) in the internal porous electrode takes places homogeneously along the entire surface domain. The remaining properties for pure gases (viscosities, heat capacities, heat capacity ratios and thermal conductivities) and hydrogen at selected temperature are collected from bibliographic data for both external and internal chambers [39]. The external and internal electrode geometries feature an axially symmetric surface which determines surface boundary conditions for gas flows and species transport models. Fig. S1 shows an (off-scale) axial cut of the SEU describing the geometry of all the domains considered in this model, the source terms and assumptions of which are collected in Table S2.

Studies performed

Previous works and projects for proton ceramic cells have found the optimal operation temperature to be 600 °C [26].

Although many have focused on designing cells for lower operation temperatures in recent years [27,28,30], a complete model and design is yet to be formulated to determine optimal device design and process conditions for operation at temperatures above and below 600 °C. Additionally, it is acknowledged for this type of tubular technology that the pressure in the external chamber of the tube cell should be equal or greater than the pressure in the internal chamber to avoid tensile stresses in the ceramic tube and seals. This means that the electrolytically produced hydrogen in this tubular cell may be compressed up to the pressure of the external chamber, but not higher. This constraint is considered throughout the entire modelling study and helps avoiding potential mechanical failure of the ceramic components and seals. In the current work, the effect of certain parameters on the system performance, such as current density, pressure in the internal and external chambers and inlet stream temperature are studied (see Table 1).

Two operation modes, mild and severe, are defined based on the pressure of the SEU chambers and water conversion, considering an inlet stream fixed at 600 °C.

1. The **mild operation mode** represents a combination of soft conditions and low steam conversion. The pressures in the steam and hydrogen chambers are set to 5 bara and 1 to 5 bara, respectively, while the steam conversion is constrained between 10 and 25%. Considering that the thermoneutral voltage must be achieved within this range of steam conversions, a large share of the inlet steam remains unconverted and absorbs the heats of the process.
2. The **severe operation mode** combines the highest operation pressures with high steam conversions. The steam and hydrogen chambers are boosted to 30 bara and 5 to 30 bara, correspondingly, with a 60–80% steam conversion. Attending to the lesser amount of unreacted gas able to absorb the generated heat, higher temperature gradients than in the previous mode can be expected.

Furthermore, the influence of the inlet temperature is also examined via a parametric study. Prescribed the same operation modes as in the previous 600 °C case, a second scenario with lower inlet stream temperature is studied to evaluate the effect of a temperature increase in an electrolysis cell operating exothermically. Table 1 collects the conditions selected for each case study. The current density response of the system to the varying conditions is in any case adjusted by the steam conversion to approach thermoneutral voltage operation.

Table 1 – Summary of the conditions studied. T_0: inlet temperature; P_{int}: pressure in the internal chamber; P_{ext}: pressure in the external chamber.

Conditions (inlet flow)	T_0 (°C)	P_{int} (bara)	P_{ext} (bara)	X (H_2O)
Evaluation of the increase of the current densityrowhead				
Mild	600	1	5	0–25
Severe	600	25	30	50–95
Evaluation of the increase of the pressure in the internal chamberrowhead				
Mild	600	1–5	5	0.2
Severe	600	5–30	30	0.8
Evaluation of the increase of the pressure in the external chamberrowhead				
Severe	600	5	5–30	0.8
Effect of the temperature of the inlet streamrowhead				
Severe	500–600	25	30	0.8

Inlet steam flows are calculated under the thermoneutral voltage operation assumption and in agreement with the selected steam conversion, X (H_2O), for each operation mode:

$$F_0(H_2O) = \frac{i_{op} \cdot Area}{z \cdot F} \cdot \frac{1}{X(H_2O)} \cdot M_{H2O} \quad (4)$$

$$F_0(O_2) = F_0(H_2O) \cdot \frac{1 - x_{0,H2O}}{x_{0,H2O}} \cdot M_{O2} \quad (5)$$

where the exchange current density, i_0, is dependent on the area specific resistance (ASR),

$$i_{op} = \frac{E_{th} - E_{rev}}{ASR_{873K}} \quad (6)$$

In addition, an oxygen molar fraction of 0.01 is set for the inlet gas to the external chamber.

Finally, a performance evaluation of the area specific resistance (ASR) of the electrochemical cell is carried out under the severe condition operating mode. The activation energy, defined by an Arrhenius expression, is computed for different ASR_{873K} values, namely 1, 2 and 3 Ω cm^2, with the correspondingly recalculated inlet stream flows presented in Table 2.

COMSOL methodology

The 2D axial symmetric model was built using COMSOL Multiphysics in steady state mode. The mesh was optimized using triangular division of the different domains. The calculations were carried out using the Parallel Direct Solver (PARDISO) with parameter continuation to assure convergence. The relative tolerance of the method was 0.001. Consistent stabilization criteria are chosen for all phenomena using streamline diffusion and crosswind diffusion. To improve the convergence of the system, the process is solved for isothermal conditions (at 600 °C), being this solution used as the initial value for the complete adiabatic process thereafter.

Fig. S2 shows the mesh used for the all-in-one tubular cell arrangement. It should be noted that the final part of the assembly (the outlet gas channels) has considered in the model. This assumption has been taken in order to simplify the model to a 2D axial symmetry. This zone can only contribute to the pressure drops since there are no mass or heat-transfer

Table 2 – Flows for the inlet stream depending on the area specific resistance of the electrochemical cell.

ASR_{873K} (Ω·cm^2)	Operation mode	$F_0(H_2O)$ (mg·min^{-1})	$F_0(O_2)$ (mg·min^{-1})
1	Severe	105	1.90
2	Severe	52.5	0.94
3	Severe	35	0.63
	Mild	205	3.70

phenomena involved in this section. The mesh is optimized using triangular forms. As can be observed from Fig. S2, the mesh gathers the nodes in the electrolyte, external electrode and in the inlet and outlet channels.

Results

Validation of model

Due to the lack of available experimental data, a set of elemental 0D models were built to control and fulfil the corroboration requirements of the COMSOL methodology and to help obtain an optimally designed electrolyte. These models consist of mass, heat and charge balances, and stand for a first order approximation for the main CDF model. The Faraday's lay was applied to assure the mass balance, considering a 100% Faradaic efficiency. The reversible voltage and ohmic losses were estimated with a 0D electrochemistry model only dependent on the inlet and outlet stream properties/partial pressures. Likewise, the preliminary energy balance was simplified to the released electrochemical energy and the inlet stream heating. The complete description of the elemental balances is provided in the supporting material and the comparison between the elemental balances and the CFD model are displayed in Fig. S3. Results disclose a robust agreement between the COMSOL model and the balances from the 0D models. These results are similar with the obtained in previous CFD works for high temperature electrolysis [26,34,40–45] (see more details in Table S4).

Analysis of the setup

To evaluate the tube-in-shell electrolysis unit, a parametric analysis of the relevant setup and performance variables governing the process is presented, considering 123 mA cm^{-2} of applied current density and mild operation conditions (Figs. 3 and 4). The steady increment of the oxygen molar fraction along the tube evidences the progressive electrochemical conversion of the steam, as it is displayed in the top profile in Fig. 3. The velocity profile of the external chamber (centre profile) reflects a smooth progression of the input flow. The slight decrease along the length of the cell, however, is ascribed to proton diffusion into the internal chamber, causing a reduction of the number of moles in the external reaction ($H_2O \rightarrow 2\,H^+ + 2\,e^- + \frac{1}{2}\,O_2$). In the case of mild operation, there is a low steam conversion of 20% and, hence, the decrease of the speed is low. The pressure variation profile in Fig. 3 (bottom) reveals the overall stable pressure with a slight drop of 10 mbar along the length of the tube (only SEU geometry).

The electrochemical potential (top) and current density (bottom) profiles of the tube-in-shell SEU module working are displayed in Fig. 4. The potential evaluation remains consistent with a small 0.02–0.03 V drop across the porous electronic conductor. This value directly depends on electronic conductivity (nominally 250 S cm^{-1} in this case). The ability of the external shell to homogenously distribute the current along the length of the external electrode is confirmed by the current density profile.

Influence of mild and severe conditions

The versatility of the electrolysis unit is manifested by the ability to operate at distinct regimes, with controlled pressures and hydrogen conversion rates. Provided a thermoneutral point at 600 °C, Fig. 5 reflects the different cell responses (temperature and cell potential) predicted for mild and severe operating conditions. While the process shifts from endothermic to exothermic modes for a current density around 120–125 mA cm^{-2} in the first scenario, the analogous turning point occurs for the second one around 70–75 mA cm^{-2} (Fig. 5a). This core discrepancy is attributed to the higher

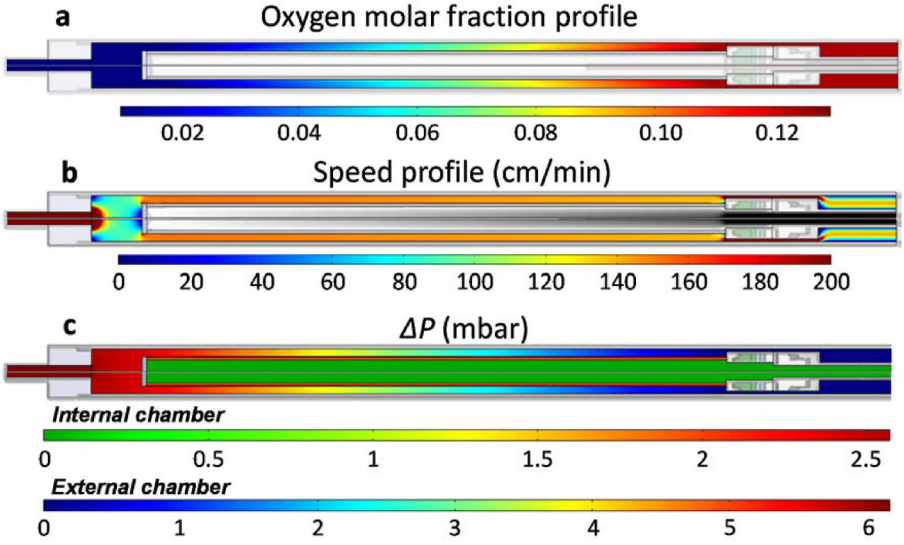

Fig. 3 – Results of the COMSOL model working under mild conditions at 123 mA cm^{-2}. Profile of the oxygen molar fraction in the external chamber (a); profile of the velocity in the external chamber (b); profiles of pressure drop in the internal chamber (c) for 1 bara in the internal chamber.

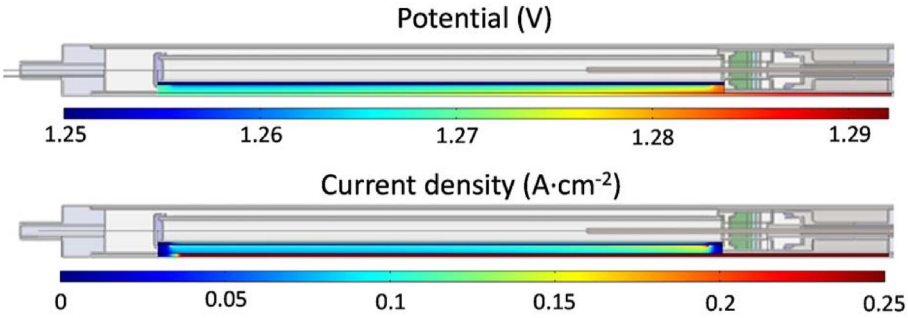

Fig. 4 – Potential and current density profiles of the COMSOL model working under mild conditions at 123 mA cm^{-2} and with1 bara in the internal chamber.

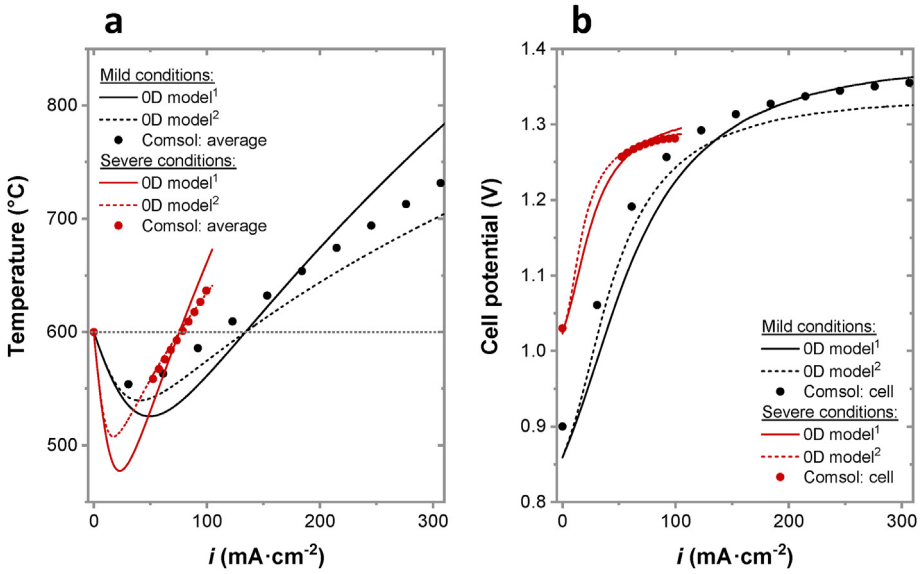

Fig. 5 – Results of the COMSOL and 0D models. Average temperature of the adiabatic process (a) and cell potential (b) as a function of the current density applied for the mild and severed conditions. [1]: 0D model with the specific resistance evaluated with the average of inlet stream and the final calculated temperature. [2]: 0D model with specific resistance evaluated with the final calculated temperature.

reversible voltage (≈1 V) of the severe with respect to the mild operation conditions, which causes thermoneutral voltage E_{th} = 1.282 V (at 600 °C) to settle at different current densities (Fig. 5b). This leads to increased hydrogen generation when compared with severe operation at the same voltages. However, the main drawbacks associated with mild operation are (i) lower pressure hydrogen generation and (ii) greater heat losses due to the high energy demand for the water vaporization combined with a low steam conversion. As Fig. 5b evidences, the stabilization of cell potentials starts once the current density surpasses the thermoneutral voltage point and is caused by an enhanced conductivity at increased temperatures. However, experimental results have shown a decrease in the faradaic efficiency at cell potentials above thermoneutral voltage [26]. The electronic leakage may be caused by increase of the cell potential and, consequently, the system will be moved to a more exothermic scenario. Therefore, a lower reversible potential is obtained at mild operation which allows the application of higher current densities than in severe conditions for the same cell potential.

Working under severe conditions makes the potential more sensitive to temperature variations compared to mild conditions, being less critical in the endothermic case. The greater fraction of unreacted gas in mild operation flow enables a superior absorption of a heat and acts as an auxiliary heat sink for the cell. Fig. 6 displays three different temperature profiles for endothermic, thermoneutral and exothermic modes in mild conditions and their corresponding current densities. Similarly, four profiles operating under severe conditions are depicted in Fig. 7, with the two latter portraying an exothermal framework. All the temperature profiles in both scenarios show relatively even distributions with low temperature gradients. It is observed that the applied current and operation voltage strongly influence the resulting temperature. Furthermore, the porous domain in the external chamber has a positive effect on heat transfer due to the presence of the external gas. However,

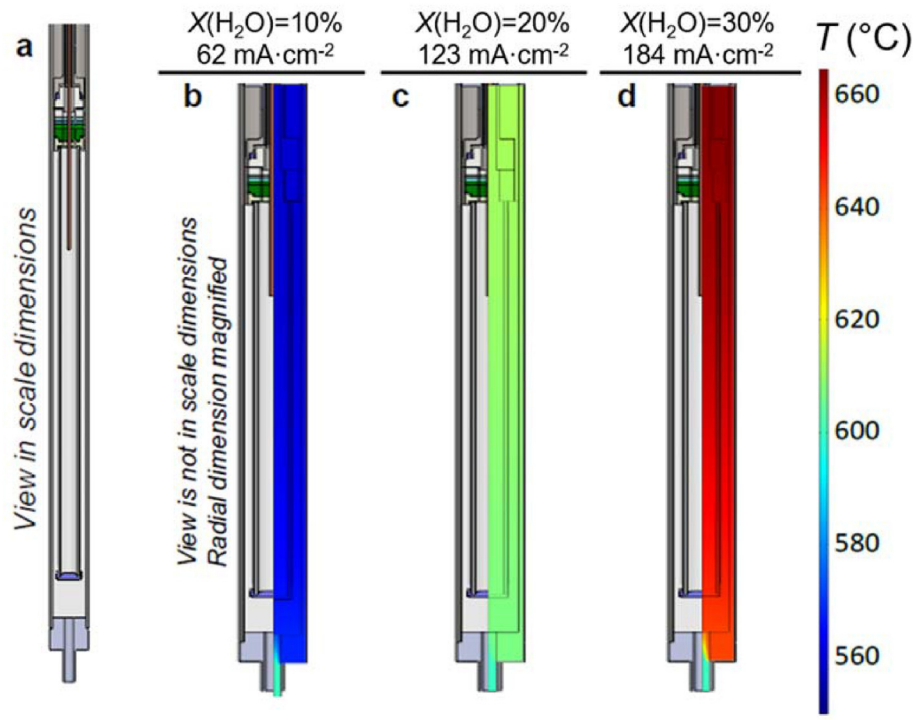

Fig. 6 – Temperature profiles of the COMSOL model working at mild operation conditions. 1 bara is used in the internal chamber. View of the setup (a), temperature profile with a steam conversion of 10% (b), 20% (c) and 30% (d).

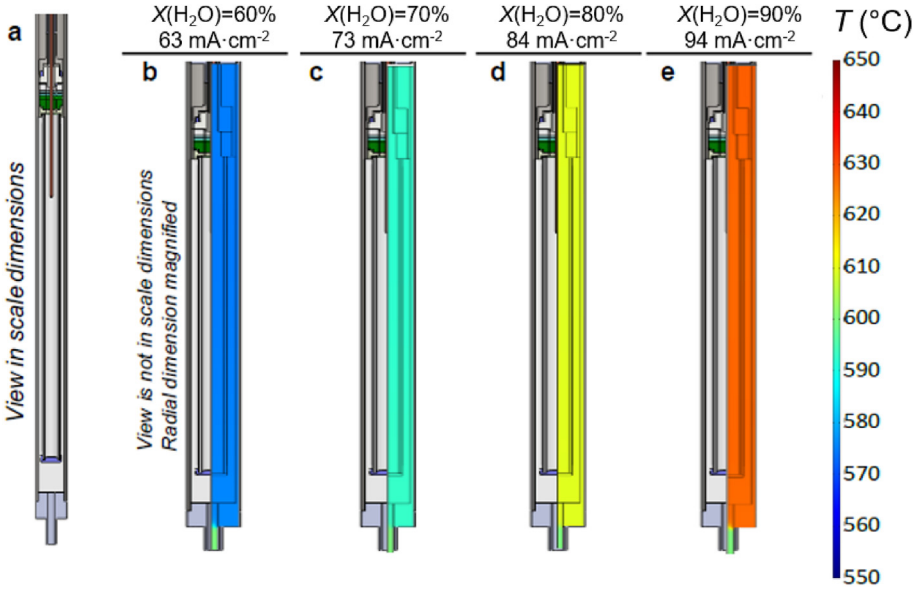

Fig. 7 – Temperature profiles of the COMSOL model of the SEU working at severe operation conditions. 25 bara is used in the internal chamber. View of the setup (a), temperature profile with a steam conversion of 60% (b), 70% (c), 80% (d) and 90% (e).

the gas flows are too low for the temperature profile to change significantly (the speed profile shows gas velocities in the range of 0.02–0.04 m s^{-1}).

H_2 pressure effect

One of the principal benefits of proton ceramic cells is their ability to produce pressurized hydrogen in a single step; however, with an associated energy cost. The influence of the hydrogen chamber's pressure on electric potential and temperature was assessed at severe operation with a current density of 79 mA cm^{-2} leading to a 75% steam conversion in the electrolysis process (Fig. 8). The associated energy cost is represented by increased reversible voltage and temperature, as evident from Fig. 8a and b, respectively. Nonetheless, the unwanted cell potential increase is partly mitigated by an

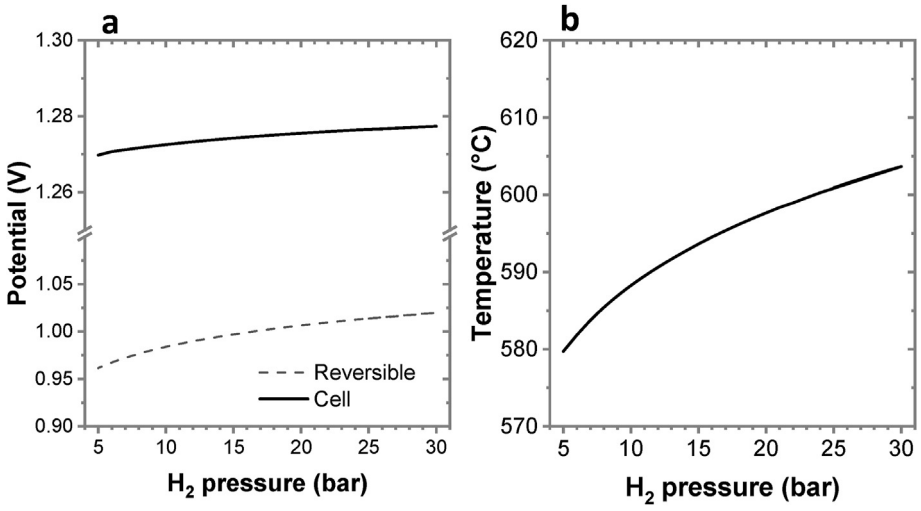

Fig. 8 – Results of the COMSOL model working at severe operation conditions. Study of the pressure of the hydrogen chamber at 79 mA cm^{-2}. Cell and reversible potentials (a) and average temperature (b) of the electrochemical cell as function of pressure in the hydrogen chamber. Potentials were evaluated considering the respective average of overall electrochemical assembly.

enhanced electrolyte conductivity at higher temperatures which leads to reduced specific resistance and corresponding lower potential and Joule heat.

Temperature profiles of the internal chamber working under severe conditions at various pressures are also studied (Fig. 9). The process shifts from the endo-to the exo-regime when the internal chamber pressure surpasses 20 bara. Therefore, low pressures in the hydrogen chamber require higher current densities to achieve thermoneutral voltage. From this, it can be derived that the cell's ability to generate hydrogen at the same potential is enhanced at lower pressures.

The effect of the increase of the H_2 pressure can be partially mitigated by increasing the pressure in the steam chamber. As can be observed in Figs. S4 and S5, the increment in the pressure of the external chamber causes a decrease in the reversible voltage, whereas the subsequent decrement in cell potential (at a fixed current density) is mitigated by the increase of the specific resistance with the reduction in cell temperature. In addition to the increase of the pressure in the steam chamber, another option to decrease the temperature of the system (in exothermic regimes) is to decrease the temperature of the feed stream. Figs. S6 and S7 show how the decrement of the resistance of the cell increases the Joule heat, despite the colder injected feed stream. Consequently, the temperature of the system does not present high decrements. The resistance of the cell increases at lower

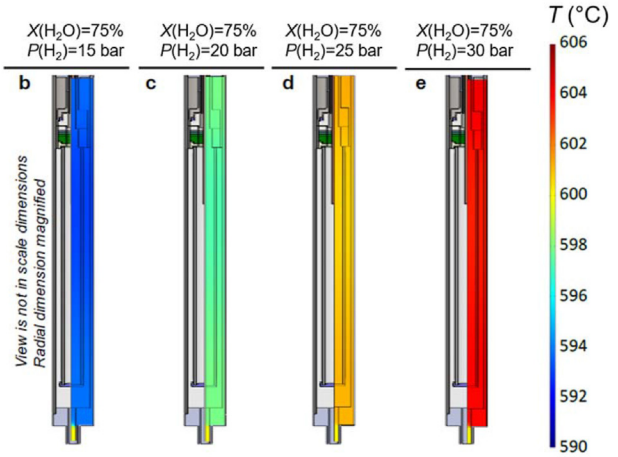

Fig. 9 – Temperature profiles of the COMSOL model working at severe operation conditions. Study of the pressure of the hydrogen chamber at 79 mA cm^{-2}.

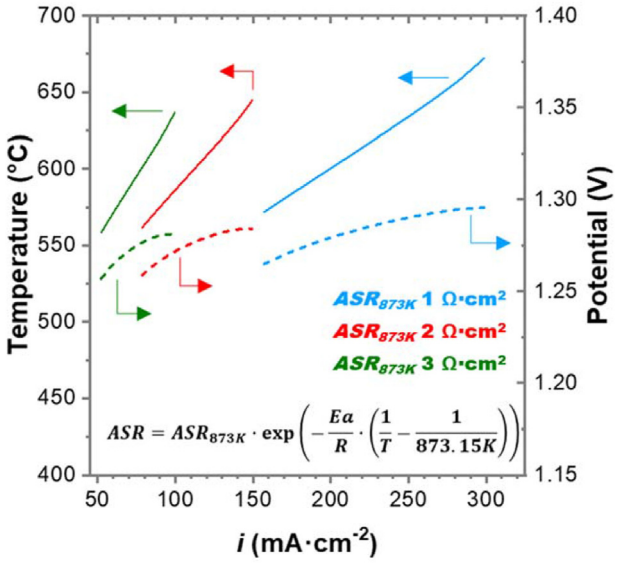

Fig. 10 – Results of the average temperature and cell potential depending on the current density model working at severe operation conditions as a function of the area specific resistance of the electrochemical cell.

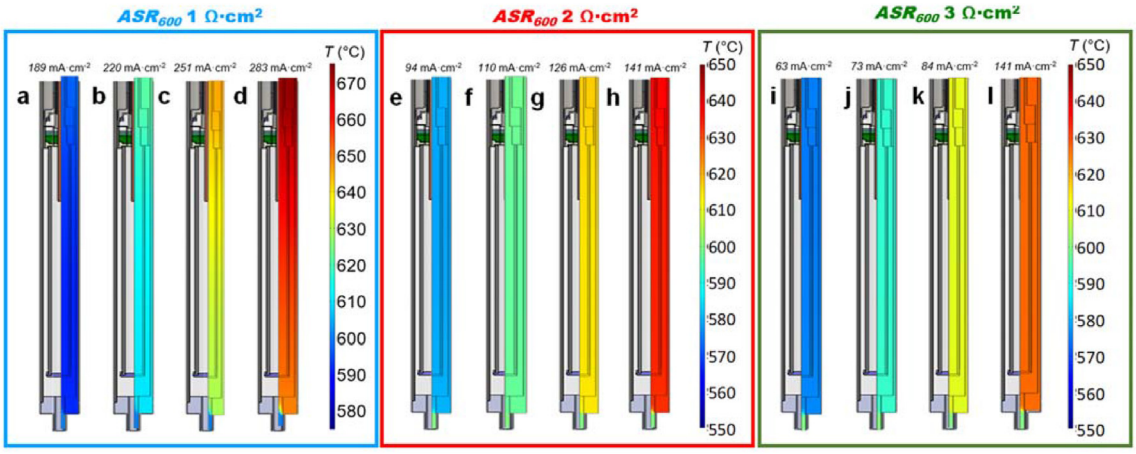

Fig. 11 – Temperature profiles of the COMSOL model at severe operation conditions as a function of the area specific resistance of the electrochemical cell.

temperatures and, consequently, it causes higher Joule heat evolution for the same current densities.

Effect of the specific resistance of the electrochemical cell

Considering the effect of the cell potential on temperature, the overall specific resistance of the cell can be identified as the principal cell parameter to be controlled. The temperatures and potentials obtained from the COMSOL models for steam conversions between 50 and 95% under severe conditions (and, consequently, the flow of the feed stream – see Table 2) at ASR of 1, 2 and 3 Ω cm^2 are presented in Fig. 10. Thermoneutral voltage is achieved at 600 °C at current densities of around 210, 120 and 75 mA cm^{-2}, respectively, and the activation energy is kept consistent in all cases. Therefore, the development of new cells with higher protonic conductivity, better electrodes and better interconnects is key to optimize the overall SEU operation. Cells with lower specific resistances allow the current density to be improved for the same cell potential and, consequently, decreasing the size of the system for the same hydrogen demands.

Finally, three sets of temperature profiles for different current densities are presented in Fig. 11, one for each evaluated ASR. It is observed that an increased ASR causes lower recorded current densities among the sets, and higher temperatures and a lower rate of hydrogen production for a given current density. Additionally, the profile at the current density of the thermoneutral point for the lower cell resistance (220 mA cm^{-2}) presents higher temperature gradients in comparison with the profiles at intermediate resistances (126 mA cm^{-2}) and the profile at high resistances (73 mA cm^{-2}). Considering that higher current densities per unit area cause a higher energy exchange, energy is more concentrated for higher current densities and, consequently, there is more heat to be transferred. Given some system, the heat displacement difficulty grows as the amount of heat involved is increased. These results emphasize the detrimental effect that an increased ASR has on the electrolysis and the overall process performance.

Conclusions

A single-tube modular electrolysis unit is designed and optimized using a CFD multi-process methodology implemented in a COMSOL Multiphysics software. The assembly is evaluated through a parametric study under two distinct operation regimes, mild and severe, attending to the steam conversion and gas pressures.

The thermoneutral voltage at a specific steam conversion is identified as a key performance value that is strongly influenced by the operating conditions and can restrict the range of hydrogen production rate of the electrolysis unit. This effect is observed in the electrochemical cell for both mild and severe operation regimes. Low steam conversions enable a better heat management and thus the operation at higher current densities, leading to smaller electrolyser area.

The effect of altering the SEU operating conditions such as internal and external chamber pressure, inlet steam temperature or area specific resistance is studied. No large gas concentration or temperature gradients are observed even at very high steam conversion rates. It is found that increasing the pressure in the internal hydrogen chamber leads to higher cell potentials and temperatures, which reduces the current density at the thermoneutral voltage and the associated hydrogen production rate. This effect can be partially mitigated by boosting the pressure of the external chamber (H_2O and O_2) and/or decreasing the temperature of the feed stream. While the pressure of the steam chamber can be easily increased using liquid water and a hydraulic pump, the electrochemical pumping through the electrolyte alleviates an additional mechanical hydrogen pressurization step. Likewise, the decrease of the feed stream temperature can provide a better heat integration of the system, providing the heat needed to achieve a sustainable thermal regime.

It was found that the utilization of a porous domain as the electronic current collector in the external chamber has a positive effect on heat transport, a major challenge in high-current electrolysers. Heat transfer is facilitated in a solid

medium (the solid phase of the porous domain) compared to a gaseous one. Indeed, the porous medium increases the interface area between solid and gas phases. This is manifested by the reduced gradient in the corresponding temperature profile.

Lastly, the influence of a critical parameter in electrolysis, i.e., the area specific resistance (ASR), was assessed. The overall resistance of the electrochemical system shifts the current density of the thermoneutral voltage. Therefore, it enables to adapt the size of the electrolyser or the hydrogen production rate depending on the application and operation regime. Cells with lower resistances per unit area allow operation at higher current densities and thus higher heat fluxes evolve. This leads to higher but acceptable temperature gradients; yet the operation remains sustainable, as Multiphysics simulations revealed, thanks to the adopted unit design.

This modelling study has shown that the designed all-in-one tubular cell assembly (SEU) based on proton ceramics for electrolysis is efficient and versatile. The overall analysis of the different profiles reveals that the process does not have fluid-dynamics or thermal limitations. The applied CFD methodology is revealed as an effective guidance for the process and geometry design as well as for material selection, leading to a successful optimization of the SEU and enabling the scaling development of electrolysers at high temperature.

Declaration of competing interest

The authors declare that they have no known competing financial interests or personal relationships that could have appeared to influence the work reported in this paper.

Acknowledgements

The work leading to these results has received funding from Spanish Government (RTI2018-102161 grant) and from Fuel Cells and Hydrogen 2 Joint Undertaking under grant agreement 779486 ('GAMER'). This Joint Undertaking receives support from the European Union's Horizon 2020 research and innovation programme, Hydrogen Europe and Hydrogen Europe research.

Appendix A. Supplementary data

Supplementary data to this article can be found online at https://doi.org/10.1016/j.ijhydene.2022.06.112.

Abbreviations and symbols

Symbol	*description*
Area	Electrochemical area (m^2)
ASR	Area specific resistance of the electrochemical cell ($\Omega \cdot m^2$)
Q_{br}	Source term of the gas flow ($kg \cdot m^{-3} \cdot s^{-1}$)
ASR_{873K}	ASR at 600 °C ($\Omega \cdot m^2$)
Q_I	Ionic current density source term ($A \cdot m^{-3}$)
CFD	Computational Fluid Dynamics
Q_S	Electronic current density source term ($A \cdot m^{-3}$)
Cp	Heat capacity ($J \cdot mol^{-1} \cdot K^{-1}$)
Q_{term}	Heat source term ($W \cdot m^{-3}$)
d_p	Particle size (m)
R	Ideal gas constant (8.314 J mol^{-1} K^{-1})
$D_{i,k}$	Gas diffusion coefficient for the i and k compounds ($m^2 \cdot s^{-1}$)
r_i	Reaction rate of the i compound ($kg \cdot m^{-3} \cdot s^{-1}$)
D_i^m	Average diffusion coefficient for the i compound ($m^2 \cdot s^{-1}$)
SEU	Single Engineering Unit
E_{cell}	Cell potential (V)
T	Temperature (K)
E_{eq}	reversible potential (V)
u	Gas velocity ($m \cdot s^{-1}$)
E_{rev}	Reversible potential (V)
w_i	Weight fraction of the i compound
E_{th}	Thermoneutral voltage (V)
$X(H_2O)$	Water conversion in the electrolysis
E_a	Energy activation of the Arrhenius expression for the ASR evaluation ($J \cdot mol^{-1}$)
x_k	Molar fraction of the k compound
F	Faraday constant (96,485 C mol^{-1})
Z	Electrons exchanged
$F_0(i)$	Mass flow of the i compound in the feeding stream ($kg \cdot s^{-1}$)
β	Exchange transference coefficient
I	Identity matrix
ΔG	Gibbs free energy ($J \cdot mol^{-1}$)
I_{op}	Total current applied (A)
ΔH	Enthalpy ($J \cdot mol^{-1}$)
i	Current density applied referred to the electrochemical area ($A \cdot m^{-2}$)
ΔS	Entropy ($J \cdot mol^{-1} \cdot K^{-1}$)
i_0	Exchange current density ($A \cdot m^{-2}$)
ϵ_p	Porosity
i_I	Ionic current density ($A \cdot m^{-2}$)
η	Overpotential (V)
i_S	Electronic current density ($A \cdot m^{-2}$)
θ_p	Solid fraction of the porous domain
j_i	Mass flux for the^i compound ($kg \cdot m^{-2} \cdot s^{-1}$)
κ	Permeability of the porous domain (m^2)
k	Thermal conductivity ($W \cdot m^{-1} \cdot K^{-1}$)
μ	Dynamic viscosity (Pa·s)
k_{eq}	Equivalent thermal conductivity for the porous domain ($W \cdot m^{-1} \cdot K^{-1}$)
ρ	Density ($kg \cdot m^{-3}$)
k_p	Thermal conductivity of the solid of the porous domain ($W \cdot m^{-1} \cdot K^{-1}$)
σ_I	Ionic conductivity ($S \cdot m^{-1}$)
M_i	Molecular weight of the i compound ($kg \cdot mol^{-1}$)
σ_S	Electronic conductivity ($S \cdot m^{-1}$)
M_n	Average molecular weight ($kg \cdot mol^{-1}$)
τ_p	Tortuosity of the porous domain
N_i	Weight flow for the i compound ($kg \cdot m^{-2} \cdot s^{-1}$)
φ_I	Ionic potential (V)

P	Total pressure (Pa or bara)
φ_S	Electronic potential (V)
p_i	Partial pressure of the i compound (Pa or bara)

Subscript description

int	internal chamber
ext	external chamber
0	feeding stream

REFERENCES

[1] Marbán G, Valdés-Solís T. Towards the hydrogen economy? Int J Hydrogen Energy 2007;32:1625–37. https://doi.org/10.1016/j.ijhydene.2006.12.017.

[2] Lymberopoulos N. Hydrogen from renewables. NATO secur. Through sci. Ser. C environ. Secur.. Dordrecht: Springer; 2007. p. 51–7. https://doi.org/10.1007/978-1-4020-6442-5_4.

[3] Armaroli N, Balzani V. The hydrogen issue. ChemSusChem 2011;4:21–36. https://doi.org/10.1002/cssc.201000182.

[4] Eberle U, Felderhoff M, Schüth F. Chemical and physical solutions for hydrogen storage. Angew Chem Int Ed 2009;48:6608–30. https://doi.org/10.1002/anie.200806293.

[5] Yang J, Sudik A, Wolverton C, Siegel DJ. High capacity hydrogen storage materials: attributes for automotive applications and techniques for materials discovery. Chem Soc Rev 2010;39:656–75. https://doi.org/10.1039/b802882f.

[6] Holladay JD, Hu J, King DL, Wang Y. An overview of hydrogen production technologies. Catal Today 2009;139:244–60. https://doi.org/10.1016/j.cattod.2008.08.039.

[7] Hosseini SE, Wahid MA. Hydrogen production from renewable and sustainable energy resources: promising green energy carrier for clean development. Renew Sustain Energy Rev 2016;57:850–66. https://doi.org/10.1016/j.rser.2015.12.112.

[8] Nikolaidis P, Poullikkas A. A comparative overview of hydrogen production processes. Renew Sustain Energy Rev 2017;67:597–611. https://doi.org/10.1016/j.rser.2016.09.044.

[9] Ruether J, Ramezan M, Grol E. Life cycle analysis of greenhouse gas emissions for hydrogen fuel production in the USA from LNG and coal. 2005.

[10] Bhandari R, Trudewind CA, Zapp P. Life cycle assessment of hydrogen production via electrolysis - a review. J Clean Prod 2014;85:151–63. https://doi.org/10.1016/j.jclepro.2013.07.048.

[11] Ahn CY, Park JE, Kim S, Kim OH, Hwang W, Her M, et al. Differences in the electrochemical performance of Pt-based catalysts used for polymer electrolyte membrane fuel cells in liquid half-and full-cells. Chem Rev 2021;121. https://doi.org/10.1021/ACS.CHEMREV.0C01337/ASSET/IMAGES/LARGE/CR0C01337_0040.JPEG.

[12] Zhou Y, Abazari R, Chen J, Tahir M, Kumar A, Ikreedeegh RR, et al. Bimetallic metal–organic frameworks and MOF-derived composites: recent progress on electro- and photoelectrocatalytic applications. Coord Chem Rev 2022;451:214264. https://doi.org/10.1016/J.CCR.2021.214264.

[13] Liu Q, Ranocchiari M, Van Bokhoven JA. Catalyst overcoating engineering towards high-performance electrocatalysis. Chem Soc Rev 2022;51:188–236. https://doi.org/10.1039/D1CS00270H.

[14] Sanati S, Abazari R, Albero J, Morsali A, García H, Liang Z, et al. Metal–organic framework derived bimetallic materials for electrochemical energy storage. Angew Chem Int Ed 2021;60:11048–67. https://doi.org/10.1002/ANIE.202010093.

[15] Abazari R, Sanati S, Morsali A. Mixed metal Fe2Ni MIL-88B metal-organic frameworks decorated on reduced graphene oxide as a robust and highly efficient electrocatalyst for alkaline water oxidation. Inorg Chem 2022;61:3396–405. https://doi.org/10.1021/ACS.INORGCHEM.1C03216/ASSET/IMAGES/LARGE/IC1C03216_0011.JPEG.

[16] Abbasi T, Abbasi SA. "Renewable" hydrogen: prospects and challenges. Renew Sustain Energy Rev 2011;15:3034–40. https://doi.org/10.1016/j.rser.2011.02.026.

[17] Ball M, Weeda M. The hydrogen economy - vision or reality? Int J Hydrogen Energy 2015;40:7903–19. https://doi.org/10.1016/j.ijhydene.2015.04.032.

[18] Götz M, Lefebvre J, Mörs F, McDaniel Koch A, Graf F, Bajohr S, et al. Renewable Power-to-Gas: a technological and economic review. Renew Energy 2016;85:1371–90. https://doi.org/10.1016/j.renene.2015.07.066.

[19] Wang M, Wang Z, Gong X, Guo Z. The intensification technologies to water electrolysis for hydrogen production - a review. Renew Sustain Energy Rev 2014;29:573–88. https://doi.org/10.1016/j.rser.2013.08.090.

[20] Zhang X, Bauer C, Mutel CL, Volkart K. Life Cycle Assessment of Power-to-Gas: approaches, system variations and their environmental implications. Appl Energy 2017;190:326–38. https://doi.org/10.1016/j.apenergy.2016.12.098.

[21] Uusitalo V, Väisänen S, Inkeri E, Soukka R. Potential for greenhouse gas emission reductions using surplus electricity in hydrogen, methane and methanol production via electrolysis. Energy Convers Manag 2017;134:125–34. https://doi.org/10.1016/j.enconman.2016.12.031.

[22] da Silva Veras T, Mozer TS, da Costa Rubim Messeder dos Santos D, da Silva César A. Hydrogen: trends, production and characterization of the main process worldwide. Int J Hydrogen Energy 2017;42:2018–33. https://doi.org/10.1016/j.ijhydene.2016.08.219.

[23] Buttler A, Spliethoff H. Current status of water electrolysis for energy storage, grid balancing and sector coupling via power-to-gas and power-to-liquids: a review. Renew Sustain Energy Rev 2018;82:2440–54. https://doi.org/10.1016/j.rser.2017.09.003.

[24] Kim J, Jun A, Gwon O, Yoo S, Liu M, Shin J, et al. Hybrid-solid oxide electrolysis cell: a new strategy for efficient hydrogen production. Nano Energy 2018;44:121–6. https://doi.org/10.1016/j.nanoen.2017.11.074.

[25] Bi L, Boulfrad S, Traversa E. Steam electrolysis by solid oxide electrolysis cells (SOECs) with proton-conducting oxides. Chem Soc Rev 2014;43:8255–70. https://doi.org/10.1039/c4cs00194j.

[26] Vøllestad E, Strandbakke R, Tarach M, Catalán-Martínez D, Fontaine M-LL, Beeaff D, et al. Mixed proton and electron conducting double perovskite anodes for stable and efficient tubular proton ceramic electrolysers. Nat Mater 2019;18:752–9. https://doi.org/10.1038/s41563-019-0388-2.

[27] Duan C, Kee R, Zhu H, Sullivan N, Zhu L, Bian L, et al. Highly efficient reversible protonic ceramic electrochemical cells for power generation and fuel production. Nat Energy 2019;4:230–40. https://doi.org/10.1038/s41560-019-0333-2.

[28] Kang EH, Choi HR, Park JS, Kim KH, Kim DH, Bae K, et al. Protonic ceramic fuel cells with slurry-spin coated BaZr0.2Ce0.6Y0.1Yb0.1O3- δ thin-film electrolytes. J Power Sources 2020;465:228254. https://doi.org/10.1016/j.jpowsour.2020.228254.

[29] Zhang JH, Lei L Bin, Liu D, Zhao FY, Chen F, Wang HQ. Numerical investigation of solid oxide electrolysis cells for hydrogen production applied with different continuity expressions. Energy Convers Manag 2017;149:646–59. https://doi.org/10.1016/j.enconman.2017.07.013.

[30] Kang J, Park J, Bae J. Three-Dimensional numerical analysis of solid oxide electrolysis cells steam electrolysis operation for hydrogen production. J Fuel Cell Sci Technol 2015;12. https://doi.org/10.1115/1.4031784.

[31] García-Camprubí M, Izquierdo S, Fueyo N. Challenges in the electrochemical modelling of solid oxide fuel and electrolyser cells. Renew Sustain Energy Rev 2014;33:701–18. https://doi.org/10.1016/j.rser.2014.02.034.
[32] Choi H-W, Pharoah JG, Ryland D, Kettner A, Gnanapragasam N. Computational fluid dynamics modeling of solid oxide electrolysis cell. ECS Trans 2013;57:3161–70. https://doi.org/10.1149/05701.3161ecst.
[33] O'Brien JE, Stoots CM, Hawkes GL. Comparison of a one-dimensional model of a high-temperature solid-oxide electrolysis stack with CFD and experimental results. In: Am. Soc. Mech. Eng. Heat transf. Div. HTD, vol. 376. HTD, American Society of Mechanical Engineers Digital Collection; 2005. p. 117–26. https://doi.org/10.1115/IMECE2005-81921.
[34] Navasa M, Yuan J, Sundén B. Computational fluid dynamics approach for performance evaluation of a solid oxide electrolysis cell for hydrogen production. Appl Energy 2015;137:867–76. https://doi.org/10.1016/j.apenergy.2014.04.104.
[35] Klein J-M, Deseure J, Bultel Y. Simulations of heat and mass transfers in tubular solid oxide electrolysis cell. ECS Trans 2019;25:1305–14. https://doi.org/10.1149/1.3205659.
[36] Hawkes GL, O'Brien JE, Stoots CM, Herring JS, Shahnam M. Computational fluid dynamics model of a planar solid-oxide electrolysis cell for hydrogen production from nuclear energy. In: Nucl. Technol., vol. 158. American Nuclear Society; 2007. p. 132–44. https://doi.org/10.13182/NT07-A3831.
[37] Ni M. 2D thermal modeling of a solid oxide electrolyzer cell (SOEC) for syngas production by H2O/CO2 co-electrolysis. Int J Hydrogen Energy 2012;37:6389–99. https://doi.org/10.1016/j.ijhydene.2012.01.072.
[38] Pianko-Oprych P, Jaworski Z, Kendall K. 13 - cell, stack and system modelling. In: Kendall K, Kendall M, editors. High-temperature solid oxide fuel cells 21st century. 2nd ed. Boston: Academic Press; 2016. p. 407–60. https://doi.org/10.1016/B978-0-12-410453-2.00013-0.
[39] Connell Jmp Bruce E Poling John O'. The properties of gases and liquids. 5th ed. New York, Chicago, San Francisco, Athens, London, Madrid, Mexico City, Milan, New Delhi, Singapore, Sydney, Toronto: McGraw-Hill Education; 2000.
[40] Hawkes G, O'Brien J, Stoots C, Hawkes B. 3D CFD model of a multi-cell high-temperature electrolysis stack. Int J Hydrogen Energy 2009;34:4189–97. https://doi.org/10.1016/j.ijhydene.2008.11.068.
[41] Herring JS, O'Brien JE, Stoots CM, Hawkes GL, Hartvigsen JJ, Shahnam M. Progress in high-temperature electrolysis for hydrogen production using planar SOFC technology. Int J Hydrogen Energy 2007;32:440–50. https://doi.org/10.1016/J.IJHYDENE.2006.06.061.
[42] Duhn JD, Jensen AD, Wedel S, Wix C. Optimization of a new flow design for solid oxide cells using computational fluid dynamics modelling. J Power Sources 2016;336:261–71. https://doi.org/10.1016/J.JPOWSOUR.2016.10.060.
[43] Hawkes GL, O'Brien JE, Tao GG. 3D CFD electrochemical and heat transfer model of an internally manifolded solid oxide electrolysis cell. In: ASME 2011 Int Mech Eng Congr Expo IMECE 2011. 4; 2012. p. 505–12. https://doi.org/10.1115/IMECE2011-62582.
[44] Celik AN. Three-dimensional multiphysics model of a planar solid oxide fuel cell using computational fluid dynamics approach. Int J Hydrogen Energy 2018;43:19730–48. https://doi.org/10.1016/J.IJHYDENE.2018.08.212.
[45] Luo Y, Shi Y, Li W, Cai N. Comprehensive modeling of tubular solid oxide electrolysis cell for co-electrolysis of steam and carbon dioxide. Energy 2014;70:420–34. https://doi.org/10.1016/J.ENERGY.2014.04.019.